

pubs.acs.org/cm Article

Studying Hydrogen—Halide Interactions in Lead Halide Perovskite with Isoelectronic Cations

Yunping Huang,* Yangwei Shi, Theodore A. Cohen, Kevin Ho, and Christine K. Luscombe



Cite This: Chem. Mater. 2023, 35, 8417-8425



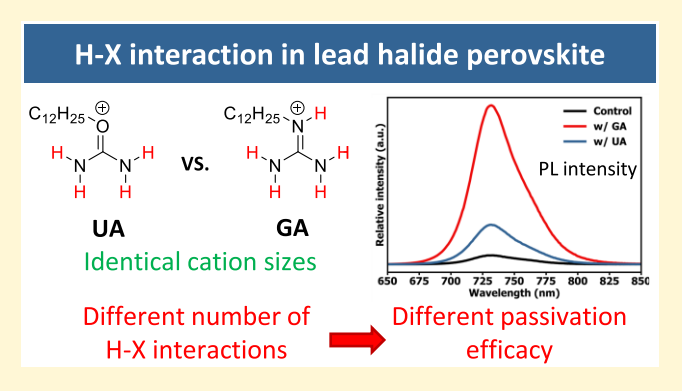
ACCESS I

III Metrics & More

Article Recommendations

Supporting Information

ABSTRACT: A-site cations in lead halide perovskite (LHP) can significantly impact the optoelectronic device efficiency and stability. These efficiency impacts have not been correlated to cation structural features because it is difficult to isolate the independent contributions from the sizes of these A-site cations and hydrogen—halide interaction between the A-site cations and PbX₆ octahedra. To address this, we designed two isoelectronic cationic ligands (guanidinium and uronium) that are nearly identical in size but have different numbers of N—H moieties that can interact with PbX₆ octahedra and studied their differences in passivating LHP solar cell interfaces. While the solar cells showed little improvement after being treated by the alkylated uronium ligand, the alkylated guanidinium ligand increased both



the fill factor (from 72.4% to ~80%) and power conversion efficiency (from 15.4% to 17.7%) compared to the untreated device, along with an increased hysteresis index (from 0.02 to 0.12). While the guanidinium-based ligand or uronium-based ligand does not have significant impacts on the morphology of the LHP, the guanidinium-based ligand demonstrated a much more pronounced effect on surface passivation of the $(Cs_{0.17}FA_{0.83})Pb(I_{0.75}Br_{0.25})_3$ films (FA = formanidinium). NMR and XRD data together suggested the guanidinium-based ligand interacts with the $(Cs_{0.17}FA_{0.83})Pb(I_{0.75}Br_{0.25})_3$ and the CsPbI $_3$ lattice with 5 H–X interactions, while the uronium-based ligand interacts with 4 due to the different lattice sizes. Raman spectra indicate that the H–X interaction between the cations and the PbX $_6$ octahedra alters the electron distribution of the resulting materials. By using a pair of isoelectronic organic cations, we excluded other variables and demonstrated the importance of the hydrogen—halide interactions between cations and PbX $_6$ octahedra on the surface passivation and optoelectronic properties of the LHP materials.

■ INTRODUCTION

A-site cations in lead halide perovskite (LHP), at first, were primarily viewed as a means to charge balance the negatively charged PbX₆ octahedra (X = Cl, Br, or I). $^{1-3}$ However, they have been found to have significant impact on the electronic structures^{4–8} and ambient stability^{9–16} of LHP materials. Cesium, methylammonium, formamidinium, and guanidinium ions are the common cations in LHPs.3 However, they have different sizes and varied numbers of hydrogen atoms interacting with the surrounding PbX₆ octahedra (as shown in Scheme 1), which leads to ambiguous results in both simulations and experiments explaining how cation size and hydrogen-halide interaction independently affect the properties of LHP materials. For example, in 2014, when Snaith et al. first used formamidinium in thin film LHP solar cells to achieve a power conversion efficiency (PCE) of 14.2%, they attributed the absorption red-shift and increased charge diffusion length to the larger size of formamidinium compared to the methylammonium.² The above hypothesis was supported by the ab initio simulation by Borriello et al. conducted in 2008 suggesting that cation size influences the electronic properties of LHP materials via modulating the deformation and tilting of the surrounding PbX₆ octahedra. On the other hand, the first-principles modeling by De Angelis et al. suggested that the improved charge transport and redshifted absorption in formamidinium lead iodide was an interplay between cation size and hydrogen—halide interaction. 4

Currently, while most of the efficient and stable LHP solar cells $^{10,14-17}$ and light-emitting diodes 11,18 are based on formamidinium and/or guanidinium instead of methylammonium when thin film LHP devices were first reported, 19 the debate on hydrogen—halide interaction in LHP materials remains highly active in both simulation $^{5-7,9,20-23}$ and experimental research. $^{6,8,11,21-25}$ Common methods include varing the cations (Cs ion, methylammonium, formamidinium,

Received: May 14, 2023 Revised: September 18, 2023 Published: October 5, 2023





Scheme 1. (a) Size Comparison of the A-Site Cations Used in LHP Perovskite; 33 (b) Synthetic Routes of GA and UA ligands

a) Size comparision of the cations used in LHP materials

Previously used cations Difference in sizes This work Nearly identical sizes

Increasing number of H-bonds

b) Synthetic routes to GA and UA ligand

and guanidinium)^{8,20,21,23,24} and/or the anions (Cl⁻, Br⁻, and I⁻)^{7–9,20,23,25} in the LHP composition, pressure,²⁵ or temperature^{21,22} to study certain trends as conditions change. However, these methods led to changes in lattice parameter^{7–9,20,23–25} or phase transitions,^{21,22,25} which impedes the correlation between LHP properties and hydrogen—halide interaction. By not controlling for other variables, these experiments sometimes lead to contradicting conclusions. For example, in the past two years, Wilks et al. indicated the existence of hydrogen—halide interaction in LHP by using density functional theory in conjunction with soft X-ray scattering,⁶ whereas a recent paper by Muydinov et al. ruled out the existence of hydrogen—halide interaction through Raman spectra and density functional theory.²¹

To address the above problems in understanding the hydrogen-halide interaction, we designed an alkylated guanidinium ligand (GA) and an alkylated uronium ligand (UA), as shown in Scheme 1, and studied their differences in interacting with the LHP lattice as a surface passivation layer. It was reported the cation radii of NH₃OH⁺ and NH₃NH₂⁺ are 216 and 217 pm, respectively. 26,27 This suggests that guanidinium and uronium can be considered as a pair of isoelectronic cations with nearly identical sizes. On the other hand, the NH group in guanidinium provides an extra site for N-H···X interaction with the surrounding PbX₆ octahedra compared to the O atom in uronium. Because urea is a very weak base with a p K_b of 13.9, compared to 2.5 of formamidine and 0.4 of guanidine, the OH group on the $C(NH_2)_2(OH)^+$ cation is considered strongly acidic and could lead to unwanted etching of the active layer. To address this, we used an alkyl chain $(-C_{12}H_{25})$ to ensure that the cation had a positive charge without acidity. We applied the same alkyl chain to the guanidinium cation to be consistent. Furthermore, these two ligands (GA and UA shown in Scheme 1) share the same counterion (methanesulfonic group). These deliberate designs allowed us to exclusively investigate the effects of the hydrogen-halide interaction in LHP without other inferences.

When we spin-coated GA and UA on top of the formamidinium-based LHP thin film in solar cell devices, GA

and UA led to drastically different results in device performance. The GA surface treatment increased the resulting solar cells' fill factor (FF) from 72.4% to 79.6% and boosted the PCE from 15.5% to 17.7%. The FF and PCE of the UA-treated device were largely unchanged. Scanning electron microscopy (SEM) and X-ray diffraction (XRD) suggest that morphological differences between the UA-passivated and GApassivated LHP films are minimal. On the other hand, ¹H nuclear magnetic resonance (NMR) and XRD together indicate (1) GA interacts with the PbX₆ in (Cs_{0.17}FA_{0.83})Pb-(I_{0.75}Br_{0.25})₃ and CsPbI₃ through 5 N-H···X interactions, while through 4 in the case of CsPbBr₃, as CsPbBr₃ has small cation sites that could only partially contain the guanidinium cation; (2) UA interacts with the PbX₆ with 4 N-H···X interactions in the case of $(Cs_{0.17}FA_{0.83})Pb(I_{0.75}Br_{0.25})_3$, CsPbBr₃ and CsPbI₃. Moreover, our Raman data indicate the N-H···X interaction between the cations and the PbX₆ octahedra changed the electron distribution and bond parameters of the guanidinium and uronium cations, and thus it is reasonable to infer that N-H···X interaction change the electron distribution of the PbX₆ octahedra as well. These results fully exclude the effects of cation size to demonstrate that hydrogen-halide interactions have a profound effect on the structural and electronic properties of LHP materials, a result that will inform further development of these important optoelectronic materials.

■ EXPERIMENTAL SECTION

Materials. All of the starting materials for ligand synthesis were used without further purification and stored under ambient conditions. Cyanamide (99%), methanesulfonic acid (99%), tetrabutylammonium hydroxide (99%), dodecyl amine (98%), and dodecanol (98%) were purchased from Sigma-Aldrich. Ethyl ether used in the precipitation and recrystallization is an ACS grade solvent.

All precursors for solar cell fabrication were used without further purification, stored, and mixed in a nitrogen-filled glovebox. Formamidinium iodide (FAI, 99.99%, Greatcell), cesium iodide (CsI, 99.999%, Sigma), lead iodide (PbI₂, 99.999%, Sigma), and lead bromide (PbBr₂, 99.999%, Sigma) were dissolved in a mixture of anhydrous *N*,*N*-dimethylformamide (DMF) and dimethyl sulfoxide (DMSO) (ratio of 4:1 v/v) to prepare a 1.45 M solution of

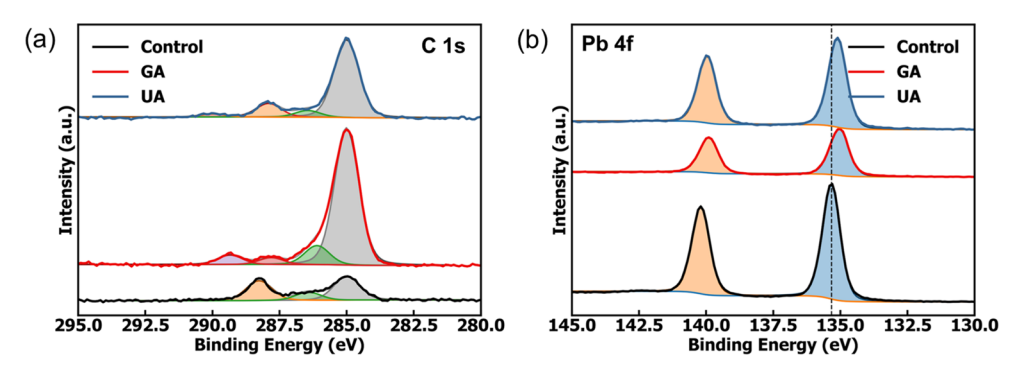


Figure 1. XPS spectra of (a) C 1s and (b) Pb 4f core levels of (Cs_{0.17}FA_{0.83})Pb(I_{0.75}Br_{0.25})₃ LHP films before and after passivation with UA or GA.

 $(Cs_{0.17}FA_{0.83})Pb(I_{0.75}Br_{0.25})_3$ according to the appropriate stoichiometric ratios.

Synthetic Procedures of Ligands. Guanidinium-Based Ligand (GA). Cyanamide (1.07 g, 25 mmol) was added to dodecyl amine (15 mL) in a round-bottomed flask with a magnetic stir bar. Methanesulfonic acid (2.4 g, 25 mmol) was added to the mixture in one portion, and the temperature of the mixture was rapidly increased. The reaction was then put into an oil bath and heated overnight at 60 °C. The next morning, the reaction was quenched by pouring ethyl ether (200 mL) into the flask and putting the flask in a freezer overnight. The white solid product was collected by filtration and dried overnight in a vacuum oven. NMR was used to determine the reaction purity, with specific screening for dodecylammonium methanesulfonic with a triplet signal at 2.74 ppm. The impurity can be easily removed by dissolving the crude product in isopropanol and adding tetrabutylammonium hydroxide (1.05 equiv to dodecylammonium methanesulfonic), followed by another recrystallization with ethyl ether. After filtration and drying, 3.2 g of product was collected as a white powder (40% yield). ¹H NMR (500 MHz, toluene- d_8) δ : 7.92 (d, J = 6.2 Hz, 1H), 7.38 (s, 4H), 3.31 (q, J = 5.8Hz, 2H), 2.82 (s, 3H), 1.69 (p, J = 7.5 Hz, 2H), 1.56–1.18 (m, 21H), 0.96 (t, J = 6.7 Hz, 3H).

Uronium-Based Ligand (UA). Cyanamide (1.07 g, 25 mmol) was added into dodecanol (15 mL) in a round-bottomed flask with a stir bar spinning. Methanesulfonic acid (2.4 g, 25 mmol) was added to the mixture in one portion, and immediately the temperature of the mixture rapidly increased. The reaction was then put into an oil bath and heated overnight at 60 °C. The next morning, the reaction was quenched by pouring into ethyl ether (200 mL) and put into the freezer overnight. White solid (crude product) was collected by filtration and dried overnight in a vacuum oven. 5.4 g of product was collected as a white powder (67% yield). ¹H NMR (500 MHz, Toluene-d8) δ: 8.68 (s, 2H), 8.31 (s, 2H), 4.45 (d, J = 7.2 Hz, 2H), 2.97 (s, 3H), 1.76 (p, J = 7.1 Hz, 2H), 1.32 (d, J = 37.0 Hz, 18H), 0.95 (dt, J = 23.0, 6.7 Hz, 3H).

Device Fabrication and Characterizations. Photoluminescence (PL) Emission and Time-Resolved PL (TRPL). An Edinburgh FLS1000 spectrometer with a PMT-980 detector was used to measure the PL emission and PL lifetime of these samples at room temperature under ambient conditions. PL emission was measured with a xenon lamp light source filtered to an excitation wavelength of 405 nm. The slit widths were the same for all of the PL measurements, which enables quantitative comparison of the PL intensities of all samples used in this work. The TRPL was performed with an EPL-405 detector and a 405 nm picosecond pulsed diode laser. The repetition rate for the TRPL is 1 MHz, which is controlled by an internal trigger input.

UV-Vis Absorption. UV-vis absorbance spectra of the perovskite films on glass substrates were measured in ambient conditions using an Agilent 8453 UV-vis spectrometer in the range 200-1100 nm.

X-ray Diffraction (XRD). We used the Bruker D8 powder X-ray diffractometer with a high-efficiency Cu anode microfocus X-ray source and an extremely sensitive Pilatus 100K large-area 2D detector

to investigate the perovskite films before and after surface treatment with GA or UA at room temperature under ambient conditions.

Solar Cell Fabrication. Patterned indium tin oxide (ITO) substrates and glass substrates were cleaned by sequential sonications in water containing ~2% Micro-90 detergent, DI water, acetone, and isopropanol (IPA) for 10 min, followed by plasma-cleaning for 5 min. The hole transport layer (HTL) used in this work is MeO-2PACz, which was dissolved in anhydrous ethanol with a concentration of 0.1 mM and spin-coated at 3000 rpm for 30 s in a nitrogen glovebox, followed by annealing at 100 °C for 10 min. The perovskite precursor solution (1.45 M) was deposited on top of the substrate and spincoated at 4000 rpm for 60 s. After ~35 s anhydrous chlorobenzene (CB) antisolvent was dispensed onto the top of the spinning substrate. The resulting perovskite films were then annealed at 100 °C for 40 min. All perovskite films were prepared in a nitrogen-filled glovebox. For surface treatment, GA and UA solutions were prepared in anhydrous IPA with a concentration of 1 or 3 mg/mL. Surface treatments were performed by dynamically depositing \sim 70 μ L of GA and UA solutions onto the perovskite films while the substrate was spun at 2000 rpm for 40 s. Afterward, the half-stack devices were transferred into an Angstrom evaporator for the deposition of C₆₀ (30 nm), BCP (5 nm), and Ag (100 nm).

Solar Cell Testing. Current—voltage (J-V) characteristics under 1 sun equivalent illumination were recorded using an ORIEL LSH-7320 ABA LED solar simulator in a nitrogen-filled glovebox, which is calibrated with a filtered KG3 silicon reference solar cell certified by NREL. Solar cells were masked during the measurement, creating an effective area of 0.0453 cm². J-V scans were performed with a Keithley 2400 instrument controlled by a program written in LabView. The voltage values are scanned at a 0.02 V step in the range of -0.1 to 1.2 V.

Scanning Electron Microscopy (SEM). SEM images were recorded with a FEI Apreo SEM at 2 kV accelerating voltage. The samples were prepared on ITO substrates to avoid charging.

Atomic Force Microscope (AFM) Modulus Measurements. The force—distance point spectra were collected using a Bruker Dimension Icon in PeakForce quantitative nanomechanical mapping (QNM) mode with a RTESPA-525 tip (k = 200 N/m, Bruker). The elastic modulus was obtained by fitting with the Hertzian model by using the Nanoscope software. Obtaining the absolute value for the Young's modulus requires a more in-depth calibration; however, the relative modulus change between the different samples is validated by using the same experimental parameters for each sample. The AFM topography was measured using an Asylum Research MFP3D mounted on an inverted optical microscope with a 75 kHz tip.

■ RESULTS AND ANALYSIS

Design and Syntheses of GA and UA. Scheme 1 summarizes the synthetic routes used to make GA and UA ligands. In the presence of methanesulfonic acid, the amine and alcohol precursors reacted with cyanamide to yield GA and UA, respectively. The reactions were completed overnight, and the final products could be easily purified through simple

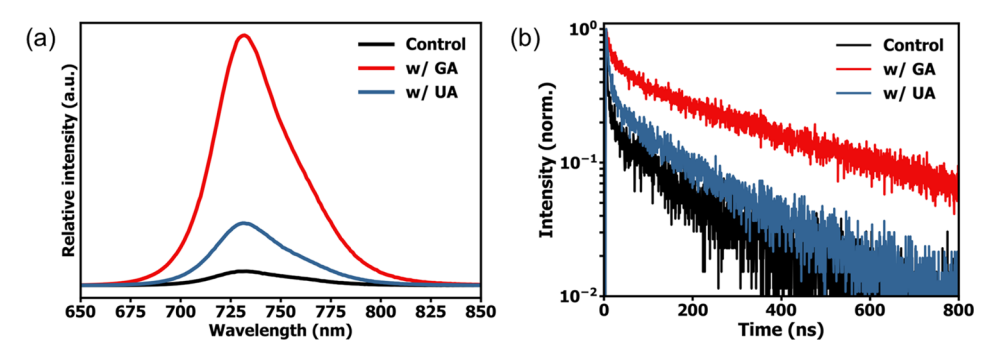


Figure 2. Comparison of PL intensity (a) and time-resolved PL decay (b) of the LHP films on glass substrates before and after surface treatment with UA or GA.

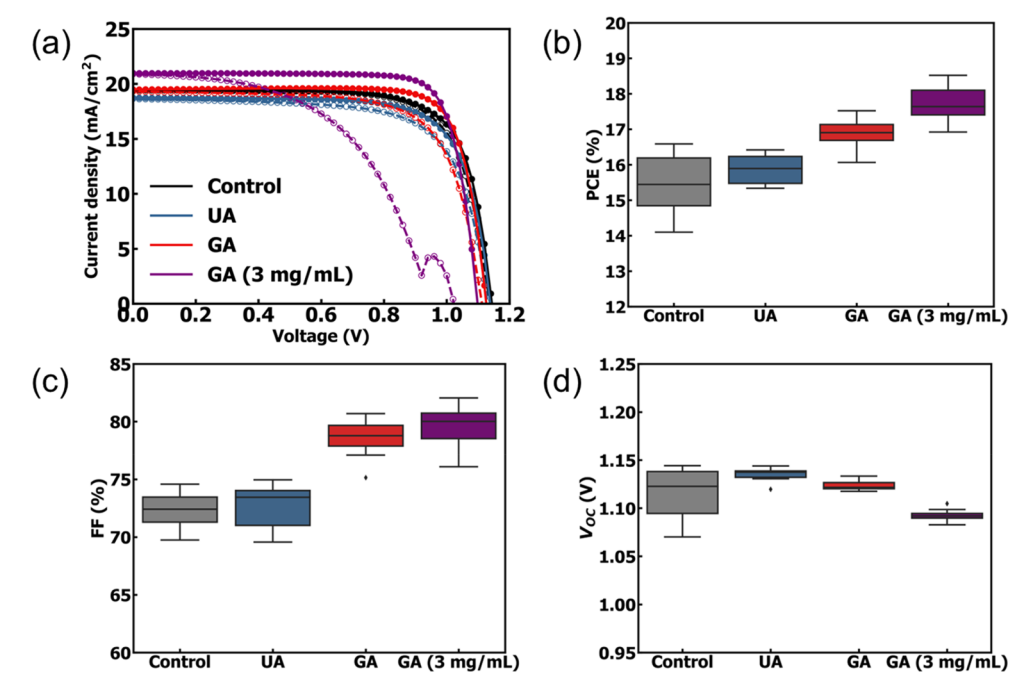


Figure 3. Performance of wide-bandgap LHP solar cells with or without ligand passivation. In the J-V curve (a), solid dots mark the reversed scan and empty dots mark the forward scan. PCE (b), FF (c), and $V_{\rm OC}$ (d) values are based on reversed scans. Detailed numbers are given in Table S1.

precipitation and recrystallization procedures. We chose the sulfonic group as the anion considering sulfonic groups have been demonstrated effective passivators for anion vacancies in LHP lattices. ^{31,32}

Different Passivation Efficacy of GA and UA in LHP Solar Cells. GA and UA were spin-coated on top of the $(Cs_{0.17}FA_{0.83})Pb(I_{0.75}Br_{0.25})_3$ LHP films. We used this methylammonium-free wide-bandgap LHP composition considering its crucial roles in stable tandem LHP solar cells^{34–36} and its tolerance factor of 0.968, which is important to circumvent undesired phase charge during surface treatment or characterization.

X-ray photoelectron spectroscopy (XPS) was used to investigate whether the ligands had attached to the perovskite surface after passivation (Figure 1). In the C 1s spectra, we observed a large intensity increase of the peak at 285 eV after passivation, indicating an increase of the sp³ C-C bond component in the UA- and GA-passivated samples. We believe this increase is from the long alkyl chains of the GA and UA ligands, while the weak sp³ C-C bond signal in the unpassivated sample is from carbon contamination. The signals with larger binding energies are from the C-N and

C–O bonds of uronium, guanidinium, and formamidinium cations. In the Pb 4f spectra, we observed the binding energy decreases by \sim 0.2 eV after passivation with UA and GA, and such shifts were observed in the I 3d and Br 3d spectra as well (Figure S1). It is hard to distinguish whether such a shift is from the passivation of the positively charged halide vacancies on the surface by CH_3SO_3^- or by the change in the surface dipole that bends the vacuum level after introducing the passivation layers.

PL and PL lifetime measurements were used for the preliminary evaluation of the ligands' efficacy in LHP surface passivation, as shown in Figure 2. After passivating the LHP film with GA, we observed a 12-fold increase in PL intensity along with an increase in PL lifetime from 134 to 337 ns compared to the untreated film. On the other hand, the passivation efficacy of UA is less pronounced, with a 5 times enhancement in the PL intensity and a slight improvement of the PL lifetime (134–176 ns). There was no shift observed in the normalized PL and normalized absorbance profiles of the LHP films before and after passivation (Figure S2), suggesting that the surface treatment has a negligible impact on the bulk perovskite optical properties.

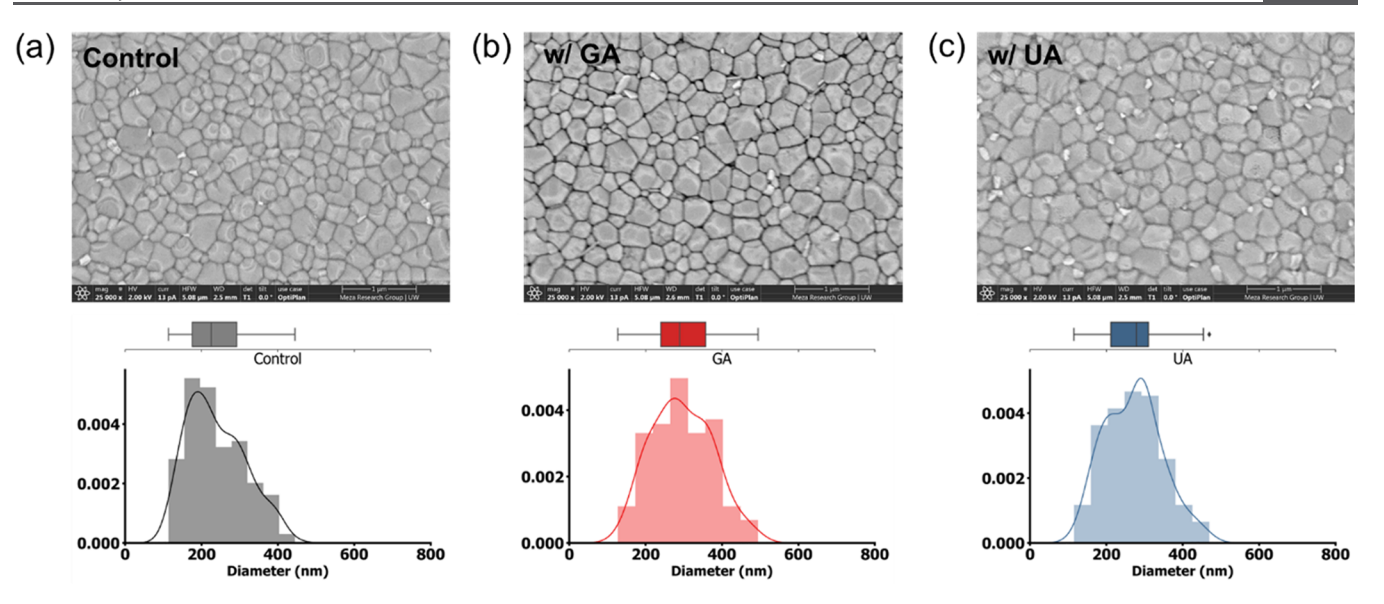


Figure 4. SEM images of (a) the as-fabricated LHP films (control) and after surface treatment with (b) GA and (c) UA (the white scale bar is 1 μ m) and their size distributions (control: 239 \pm 75 nm; GA: 295 \pm 79 nm; UA: 271 \pm 74 nm).

We then fabricated solar cell devices with or without GAtreated LHP films. Figure 3 shows the performance of the respective devices, and the GA-passivated LHP films showed the best performance among the three devices. When the concentrations of the ligand solutions were 1 mg/mL, we observed a significant increase in the fill factor (FF) of the GApassivated device, to an average of 78.7% from 72.4% of the untreated devices. On the other hand, we observed a slight drop in the open-circuit voltage (V_{OC}) in the GA-passivated devices, from 1.13 to 1.12 V, while the change in short-circuit current (J_{SC}) was negligible. As a result, the power-conversion efficiency (PCE) of the GA-passivated devices was mildly increased to 16.9% compared with 15.5% of the unpassivated references. However, the changes in FF, V_{OC} , and J_{SC} in UAtreated devices were insignificant, and thus the average PCE of the UA-treated devices is similar to the reference devices without surface treatment. The J_{SC} of both devices remains nearly unchanged compared to untreated devices, which is consistent with other reports of LHP solar cells passivated with a long or bulky insulating side chain.³⁷⁻³⁹ When we further increased the concentration of the GA ligand to 3 mg/mL, we observed a further increase in J_{SC} and FF, to 20.4 mA cm⁻² and 79.6%, respectively, leading to a PCE of ~18%, along with a high hysteresis index of 0.41. Our mechanistic hypothesis of the mechanism of the high hysteresis of the GA-treated solar cells will be discussed later in the paper.

These drastically different solar cell performance indicate that GA and UA adopt different mechanisms for LHP thin-film passivation. Considering their nearly identical sizes, we believe that the greater N–H···X interactions between the cation and the PbX₆ octahedra lead to better LHP passivation. Therefore, in the next section, we evaluate this hypothesis using XRD, SEM, NMR, and Raman spectra to investigate the interaction mechanism between the ligands and the LHP films.

Understanding the Interactions between the LHP Lattices and Cations. We first used SEM to study the morphology of the LHP films before and after passivation, considering it is widely observed that post-treatments with ligands often modify the morphology of the LHP films. 40,41 As shown in Figure 4, the grain size of the LHP films slightly

increased after UA or GA treatment, and the average grain sizes of the UA- and GA-treated films are very comparable. This result excludes differences in grain sizes as the origin of the better efficacy of GA in LHP thin film passivation.

Cations with long alkyl chains have been exploited to passivate LHP thin films by forming 2D perovskites at grain boundaries. 42–44 Due to the difference in lattice parameters between 2D and 3D perovskites, XRD is commonly used to probe the existence of 2D perovskites at interfaces. However, as shown in Figure 5, the XRD patterns before and after ligand

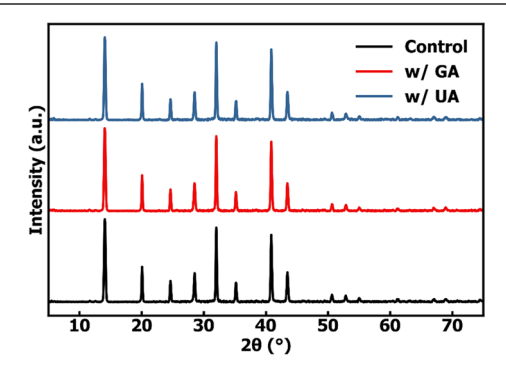


Figure 5. XRD patterns of the LHP thin film with and without surface treatment.

treatments are nearly identical. This experiment shows that the ligand treatment does not modify the perovskite crystal structure in a way that can be detected by this measurement and rules out the passivation mechanism of the 2D perovskite formation at the interface.

Despite the significant differences in optoelectronic performances (PL intensity, PL lifetime, PCE, and hysteresis), crystallinity and morphology characterizations with XRD and SEM showed the morphologies of the UA- and GA-passivated films are very similar. We thus used NMR and Raman spectra to study the N-H···X interaction between the LHP lattice and GA and UA on a molecular interaction level. In the NMR and Raman experiments, cesium lead halide nanocrystals (NCs) were used instead of LHP thin films in the experiment (1) to

obtain clear NMR signals via a solution-based NMR technique and (2) to eliminate the interference of formamidinium signals within crystal grain to exclusively study the ligand—LHP interaction at the surface, where the passivation takes place. Figure 6 compares the ¹H NMR spectra of the GA and UA

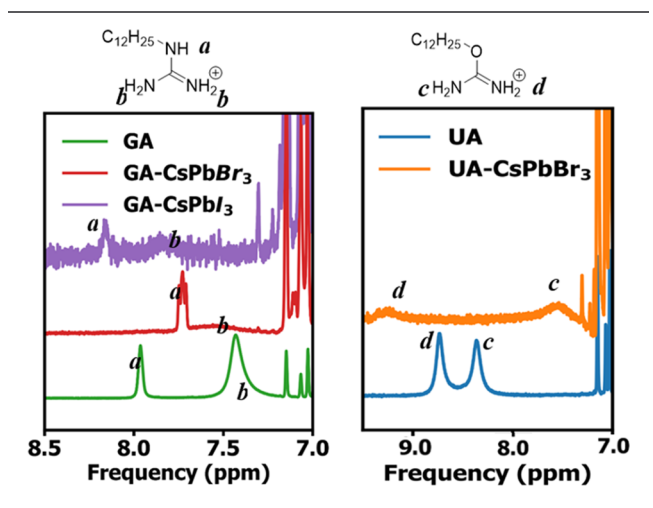


Figure 6. ¹H NMR spectra of the GA and UA ligands, GA-passivated CsPbI₃ NCs, GA-passivated CsPbBr₃ NCs, and UA-passivated CsPbBr₃ NCs, taken at room temperature with toluene-*d*₈ as the solvent. The broadening of the NMR peaks indicates that the hydrogen atoms interact with the LHP lattice. The NH in the GA-CsPbBr₃ sample remains sharp compared to the NH₂ peaks, indicating no direct interaction with the LHP lattice.

ligands and their passivated cesium lead halide NCs. The broadening of the NH₂ and NH signals in the GA-passivated CsPbI₃ NCs indicates that both the NH₂ and NH groups are interacting with adjacent PbI₆ octahedra. Although GA is larger than the common cations used in LHP, the NMR results presented above show that the whole guanidinium cation could fit into the cation site of the CsPbI₃ lattice. On the other hand, the guanidinium cation could only partially fit into the cation site of the CsPbBr₃ lattice; as shown in the NMR only the NH₂ signals are broadened. All of the NH2 signals of UA are broadened after being incorporated into the CsPbBr₃ lattice. It is worth mentioning that we were not able to perform ligand exchange with CsPbI₃ NCs, as UA induced a transformation to the non-perovskite yellow phase. Considering the position of the (100) diffraction peaks of CsPbBr₃ and CsPbI₃ are respectively 14.9° and 14.4°, 45,46 while it is 14.1° for $(Cs_{0.17}FA_{0.83})Pb(I_{0.75}Br_{0.25})_3$ (Figure 5), $(Cs_{0.17}FA_{0.83})Pb$ -(I_{0.75}Br_{0.25})₃ possesses larger lattice parameters compared to CsPbI₃, which means that the guanidinium cation can fully fit into the cation site of $(Cs_{0.17}FA_{0.83})Pb(I_{0.75}Br_{0.25})_3$. In addition, we observed a small decrease in the $V_{\rm OC}$ in the GA-passivated solar cells, which could be attributed to the extra N-H···X interaction between guanidinium and PbX6 octahedra that promotes spin-orbit coupling in LHP and narrows its bandgap.

Raman spectra were used to further investigate the interaction between the ligands and the perovskite lattice, and results are shown in Figure 7. We used $CsPbBr_3$ for this analysis because the 785 m laser used in our Raman setup is close to the bandgap of $(Cs_{0.17}FA_{0.83})Pb(I_{0.75}Br_{0.25})_3$. This led to strong fluorescence that impeded our ability to effectively characterize the material with this technique. The $CsPbBr_3$ thin film sample, which has no ligand, shows no significant

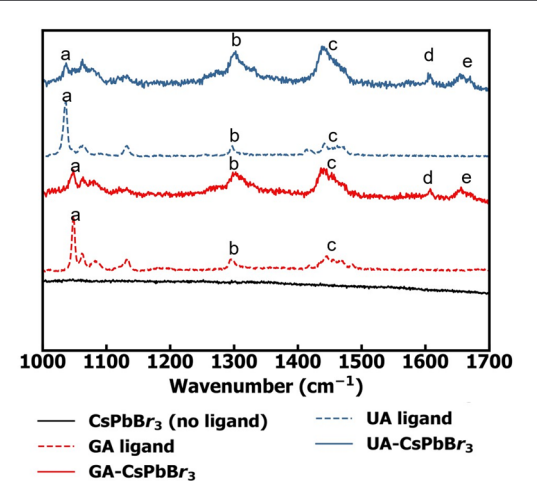


Figure 7. Raman spectra of the different ligands and $CsPbBr_3$ samples. Peak attribution: (a) symmetric stretching of CN_3 and CN_2O , (b) CH_2 twisting, (c) CH_2 scissoring, (d) NH_2 scissoring, and (e) asymmetric stretching of CN_3 and CN_2O .

peaks across the 250-2250 cm⁻¹ range. The free UA and free GA ligands show very similar Raman profiles due to their isoelectronic nature (see Figure S4 for the full spectra). According to Sension et al.,47 in the free ligand spectra of GA and UA, the sharp peaks around 1037 and 1048 cm⁻¹ originate from the symmetric in-plane stretching of the CN₃ and CN₂O skeleton of guanidinium and uronium, respectively. When UA and GA interact with the CsPbBr3 lattice, we observe a significant reduction in the intensity of CN₃ and CN₂O symmetric stretching, with the appearance of the two new peaks at 1610 and 1658 cm⁻¹, which originate respectively from the scissoring of NH₂²⁴ and the asymmetric out-of-plane stretching of the CN₃ and CN₂O skeleton. The above results indicate that the H-X interactions between the cations and the PbX₆ octahedra have changed the electron distribution of the cations, which means it is reasonable to infer that such interactions change the electron distribution of the PbX₆ octahedra as well. On the other hand, the change in the CH₂ signals is insignificant, ⁴⁸ indicating that the alkyl chains have trivial interaction with the perovskite lattice.

Such an interaction between the cation ligand and the PbX₆ octahedron could explain the high hysteresis in the GApassivated device, as ligands have a significant impact on the mobility and diffusivity of surface ions on the inorganic crystals. Nelson et al. investigated optoelectronic behaviors of PbS quantum dots (Pb²⁺-rich surface) capped with carboxylate, amine, and thiolate ligands. 49 Due to the strong interaction between thiolate and Pb2+ (comparable Pb-S interaction within the QD lattice), the thiolate ligands were able to extract the Pb²⁺ from the QD surface via coordination. Furthermore, the mobility of the alkyl chain allows the extracted Pb ²⁺ to further diffuse into the ligand layer and create trap states at the interface, which was evidenced by the formation of a lowintensity PL peak at longer wavelengths at room temperature. However, both carboxylate and amine bind weakly to Pb²⁺, and they are not able to compete with the Pb-S interaction within the OD lattice. Therefore, neither carboxylate nor amine ligands can extract Pb2+ from the QD surface, and no trap-state emission was observed. The above interaction mechanism between the inorganic lattice and weakly/strongly binding ligands could explain the mechanisms of the more pronounced hysteresis in the GA-treated LHP sample. While GA interacts

with PbX_6 octahedra with 5 hydrogen atoms, UA and the formamidinium interact with 4. GA binds to the PbX_6 octahedra more strongly than the formamidinium within the perovskite grain and can extract the PbX_6 octahedra from the inorganic lattice. Along with the mobility endowed by the long alkyl chain, the PbX_6 octahedra can rearrange easily at the GA-passivated interface, which could lead to more pronounced hysteresis in solar cell devices (Figure 3). Moreover, the hysteresis index was further increased when the GA concentration was increased from 1 to 3 mg/mL. The UA— PbX_6 interaction and formamidinium— PbX_6 interaction are of similar strength, and thus, we observed a relatively smaller hysteresis in the UA-treated device, which however is still higher than the ones of the untreated solar cells.

CONCLUSION

In conclusion, by using a pair of isoelectronic organic cations (GA and UA), we excluded other variables to only study how the hydrogen-halide interactions between cations and PbX₆ octahedra affect the surface passivation and the optoelectronic properties of LHP materials. While GA and UA do not significantly change the morphology of the LHP, GA had a much more pronounced effect on surface passivation of the $(Cs_{0.17}FA_{0.83})Pb(I_{0.75}Br_{0.25})_3$ films. NMR showed GA interacts with the $(Cs_{0.17}FA_{0.83})Pb(I_{0.75}Br_{0.25})_3$ lattice with 5 H-X interactions while UA interacts with 4, and Raman spectra indicated that the H-X interaction between the cations and the PbX₆ octahedra could alter the electron distribution and the bond parameters of the resulting materials. The findings presented above indicate that H-X interactions between cations and PbX₆ octahedra play a key role in the properties of LHP materials.

ASSOCIATED CONTENT

Supporting Information

The Supporting Information is available free of charge at https://pubs.acs.org/doi/10.1021/acs.chemmater.3c01149.

NMR spectra, XPS, UV-vis, and AFM images (PDF)

AUTHOR INFORMATION

Corresponding Author

Yunping Huang — Department of Materials Science and Engineering, University of Washington, Seattle, Washington 98195, United States; orcid.org/0000-0001-8461-7160; Email: YUNPING.HUANG@COLORADO.EDU

Authors

Yangwei Shi — Molecular Engineering & Sciences Institute and Department of Chemistry, University of Washington, Seattle, Washington 98195, United States; orcid.org/0000-0002-9014-7422

Theodore A. Cohen – Molecular Engineering & Sciences Institute, University of Washington, Seattle, Washington 98195, United States; oorcid.org/0000-0001-7170-3211

Kevin Ho – Department of Chemistry, University of Washington, Seattle, Washington 98195, United States; orcid.org/0000-0003-2688-2606

Christine K. Luscombe — Department of Materials Science and Engineering, University of Washington, Seattle, Washington 98195, United States; Molecular Engineering & Sciences Institute and Department of Chemistry, University of Washington, Seattle, Washington 98195, United States; piConjugated Polymers Unit, Okinawa Institute of Science and Technology, Okinawa 904-0495, Japan; ocid.org/0000-0001-7456-1343

Complete contact information is available at: https://pubs.acs.org/10.1021/acs.chemmater.3c01149

Author Contributions

Y.H. and Y.S. contributed equally to this work. Y.H. conceived this idea, synthesized the ligands, designed experiments, and took the lead in writing the manuscript. Y.S. fabricated and characterized the solar cell devices and conducted ABS, PL, PL lifetime, SEM, and XRD experiments. T.A.C. synthesized the nanoparticles and conducted the NMR studies before and after ligand exchange. Kevin Ho measured Young's modulus with AFM. C.K.L. supervised this project.

Notes

The authors declare no competing financial interest.

ACKNOWLEDGMENTS

This research was supported by the National Science Foundation (NSF) through the UW Molecular Engineering Materials Center, a Materials Research Science and Engineering Center (DMR-1719797 to C.K.L.). The authors also acknowledge the financial support from the Clean Energy Institute (C.K.L.). Y.S. acknowledges the financial support from the Office of Naval Research (ONR), Award N00014-20-1-2587. K.H. is supported by DOE BES under Award DE-SC0013957. Part of this work was performed at the Washington Nanofabrication Facility/Molecular Analysis Facility, a National Nanotechnology Coordinated Infrastructure (NNCI) site at the University of Washington with partial support from the National Science Foundation via Awards NNCI-2025489 and NNCI-1542101. Y.H. thanks Prof. Brandi M. Cossairt for her comment on isolating the contributions of hydrogen-halide interaction from others at the beginning of this project and Prof. David S. Ginger for his support, suggestions, and use of facility to perform this work and Prof. Daniel R. Gamelin for letting us use facilities in his laboratories.

REFERENCES

- (1) Borriello, I.; Cantele, G.; Ninno, D. Ab Initio Investigation of Hybrid Organic-Inorganic Perovskites Based on Tin Halides. *Phys. Rev. B Condens. Matter Mater. Phys.* **2008**, 77 (23), 235214.
- (2) Eperon, G. E.; Stranks, S. D.; Menelaou, C.; Johnston, M. B.; Herz, L. M.; Snaith, H. J. Formamidinium Lead Trihalide: A Broadly Tunable Perovskite for Efficient Planar Heterojunction Solar Cells. *Energy. Environ. Sci.* **2014**, *7*, 982.
- (3) Lu, C.-H.; Biesold-Mcgee, G. v; Liu, Y.; Kang, Z.; Lin, Z. Doping and Ion Substitution in Colloidal Metal Halide Perovskite Nanocrystals. *Chem. Soc. Rev.* **2020**, *49*, 4953.
- (4) Amat, A.; Mosconi, E.; Ronca, E.; Quarti, C.; Umari, P.; Nazeeruddin, M. K.; Gratzel, M.; De Angelis, F. Cation-Induced Band-Gap Tuning in Organohalide Perovskites: Interplay of Spin-Orbit Coupling and Octahedra Tilting. *Nano Lett.* **2014**, *14*, 3608.
- (5) Varadwaj, A.; Varadwaj, P. R.; Marques, H. M.; Yamashita, K. Halogen in Materials Design: Revealing the Nature of Hydrogen Bonding and Other Non-Covalent Interactions in the Polymorphic Transformations of Methylammonium Lead Tribromide Perovskite. *Mater. Today. Chem.* **2018**, *9*, 1.
- (6) Wilks, R. G.; Erbing, A.; Sadoughi, G.; Starr, D. E.; Handick, E.; Meyer, F.; Benkert, A.; Iannuzzi, M.; Hauschild, D.; Yang, W.; Blum, M.; Weinhardt, L.; Heske, C.; Snaith, H. J.; Odelius, M.; Bär, M.

Dynamic Effects and Hydrogen Bonding in Mixed-Halide Perovskite Solar Cell Absorbers. J. Phys. Chem. Lett. 2021, 12, 3885.

- (7) Kanno, S.; Imamura, Y.; Hada, M. First-Principles Calculations of the Rotational Motion and Hydrogen Bond Capability of Large Organic Cations in Hybrid Perovskites. *J. Phys. Chem. C* **2018**, *122*, 15966.
- (8) Kamal, C.; Hauschild, D.; Seitz, L.; Steininger, R.; Yang, W.; Heske, C.; Weinhardt, L.; Odelius, M. Coupling Methylammonium and Formamidinium Cations with Halide Anions: Hybrid Orbitals, Hydrogen Bonding, and the Role of Dynamics. *J. Phys. Chem. C* **2021**, 125, 25917.
- (9) El-Mellouhi, F.; Marzouk, A.; Bentria, E. T.; Rashkeev, S. N.; Kais, S.; Alharbi, F. H. Hydrogen Bonding and Stability of Hybrid Organic-Inorganic Perovskites. *ChemSusChem* **2016**, *9*, 2648.
- (10) Jodlowski, A. D.; Roldán-Carmona, C.; Grancini, G.; Salado, M.; Ralaiarisoa, M.; Ahmad, S.; Koch, N.; Camacho, L.; de Miguel, G.; Nazeeruddin, M. K. Large Guanidinium Cation Mixed with Methylammonium in Lead Iodide Perovskites for 19% Efficient Solar Cells. *Nature Energy* **2017**, *2* (12), 972.
- (11) Kim, Y. H.; Kim, S.; Kakekhani, A.; Park, J.; Park, J.; Lee, Y. H.; Xu, H.; Nagane, S.; Wexler, R. B.; Kim, D. H.; Jo, S. H.; Martínez-Sarti, L.; Tan, P.; Sadhanala, A.; Park, G. S.; Kim, Y. W.; Hu, B.; Bolink, H. J.; Yoo, S.; Friend, R. H.; Rappe, A. M.; Lee, T. W. Comprehensive Defect Suppression in Perovskite Nanocrystals for High-Efficiency Light-Emitting Diodes. *Nat. Photonics* **2021**, *15*, 148.
- (12) Protesescu, L.; Yakunin, S.; Kumar, S.; Bar, J.; Bertolotti, F.; Masciocchi, N.; Guagliardi, A.; Grotevent, M.; Shorubalko, I.; Bodnarchuk, M. I.; Shih, C.-J.; Kovalenko, M. V. Dismantling the "Red Wall" of Colloidal Perovskites: Highly Luminescent Formamidinium and Formamidinium-Cesium Lead Iodide Nanocrystals. *ACS Nano* 2017, 11, 3119.
- (13) Meng, X.; Lin, J.; Liu, X.; He, X.; Wang, Y.; Noda, T.; Wu, T.; Yang, X.; Han, L. Highly Stable and Efficient FASnI3-Based Perovskite Solar Cells by Introducing Hydrogen Bonding. *Adv. Mater.* **2019**, *31*, 1903721.
- (14) He, X.; Chen, J.; Ren, X.; Zhang, L.; Liu, Y.; Feng, J.; Fang, J.; Zhao, K.; Liu, S. 40.1% Record Low-Light Solar-Cell Efficiency by Holistic Trap-Passivation Using Micrometer-Thick Perovskite Film. *Adv. Mater.* **2021**, 33, 202100770.
- (15) Mozaffari, N.; Duong, T.; Shehata, M. M.; Bui, A. D.; Pham, H. T.; Yin, Y.; Mayon, Y. O.; Zheng, J.; Mahmud, M. A.; Tabi, G. D.; Andersson, G. G.; Black, L. E.; Peng, J.; Shen, H.; White, T. P.; Weber, K.; Catchpole, K. R. Above 23% Efficiency by Binary Surface Passivation of Perovskite Solar Cells Using Guanidinium and Octylammonium Spacer Cations. *Solar RRL* 2022, *6*, 202200355.
- (16) Tong, J.; Jiang, Q.; Ferguson, A. J.; Palmstrom, A. F.; Wang, X.; Hao, J.; Dunfield, S. P.; Louks, A. E.; Harvey, S. P.; Li, C.; Lu, H.; France, R. M.; Johnson, S. A.; Zhang, F.; Yang, M.; Geisz, J. F.; McGehee, M. D.; Beard, M. C.; Yan, Y.; Kuciauskas, D.; Berry, J. J.; Zhu, K. Carrier Control in Sn-Pb Perovskites via 2D Cation Engineering for All-Perovskite Tandem Solar Cells with Improved Efficiency and Stability. *Nature Energy* 2022, 7, 642.
- (17) Min, H.; Lee, D. Y.; Kim, J.; Kim, G.; Lee, K. S.; Kim, J.; Paik, M. J.; Kim, Y. K.; Kim, K. S.; Kim, M. G.; Shin, T. J.; il Seok, S. Perovskite Solar Cells with Atomically Coherent Interlayers on SnO₂ Electrodes. *Nature* **2021**, *598*, 444.
- (18) Kim, Y. H.; Park, J.; Kim, S.; Kim, J. S.; Xu, H.; Jeong, S. H.; Hu, B.; Lee, T. W. Exploiting the Full Advantages of Colloidal Perovskite Nanocrystals for Large-Area Efficient Light-Emitting Diodes. *Nat. Nanotechnol.* **2022**, *17*, 590.
- (19) Lee, M. M.; Teuscher, J.; Miyasaka, T.; Murakami, T. N.; Snaith, H. J. Efficient Hybrid Solar Cells Based on Meso-Super-structured Organometal Halide Perovskites. *Science* **2012**, 338, 643.
- (20) Svane, K. L.; Forse, A. C.; Grey, C. P.; Kieslich, G.; Cheetham, A. K.; Walsh, A.; Butler, K. T. How Strong Is the Hydrogen Bond in Hybrid Perovskites? *J. Phys. Chem. Lett.* **2017**, *8*, 6154.
- (21) Ibaceta-Jaña, J.; Chugh, M.; Novikov, A. S.; Mirhosseini, H.; Kühne, T. D.; Szyszka, B.; Wagner, M. R.; Muydinov, R. Do Lead

- Halide Hybrid Perovskites Have Hydrogen Bonds? J. Phys. Chem. C 2022, 126, 16215.
- (22) Yin, T.; Fang, Y.; Fan, X.; Zhang, B.; Kuo, J. L.; White, T. J.; Chow, G. M.; Yan, J.; Shen, Z. X. Hydrogen-Bonding Evolution during the Polymorphic Transformations in CH3NH3PbBr3: Experiment and Theory. *Chem. Mater.* **2017**, *29*, 5974.
- (23) Ibaceta-Jaña, J.; Muydinov, R.; Rosado, P.; Mirhosseini, H.; Chugh, M.; Nazarenko, O.; Dirin, D. N.; Heinrich, D.; Wagner, M. R.; Kühne, T. D.; Szyszka, B.; Kovalenko, M. v.; Hoffmann, A. Vibrational Dynamics in Lead Halide Hybrid Perovskites Investigated by Raman Spectroscopy. *Phys. Chem. Chem. Phys.* **2020**, 22, 5604.
- (24) Ruan, S.; McMeekin, D. P.; Fan, R.; Webster, N. A. S.; Ebendorff-Heidepriem, H.; Cheng, Y. B.; Lu, J.; Ruan, Y.; McNeill, C. R. Raman Spectroscopy of Formamidinium-Based Lead Halide Perovskite Single Crystals. *J. Phys. Chem. C* **2020**, *124*, 2265.
- (25) Wang, L.; Wang, K.; Xiao, G.; Zeng, Q.; Zou, B. Pressure-Induced Structural Evolution and Band Gap Shifts of Organometal Halide Perovskite-Based Methylammonium Lead Chloride. *J. Phys. Chem. Lett.* **2016**, *7*, 5273.
- (26) Kieslich, G.; Sun, S.; Cheetham, A. K. Solid-State Principles Applied to Organic-Inorganic Perovskites: New Tricks for an Old Dog. *Chem. Sci.* **2014**, *5*, 4712.
- (27) Kieslich, G.; Sun, S.; Cheetham, A. K. An Extended Tolerance Factor Approach for Organic-Inorganic Perovskites. *Chem. Sci.* **2015**, *6*, 3430.
- (28) Perrin, D. D. (1965) Dissociation Constants of Organic Bases in Aqueous Solution. Butterworths, London (Supplement, 1972). References Scientific Research Publishing. https://www.scirp.org/(S(351jmbntvnsjt1aadkposzje))/reference/ReferencesPapers.aspx?ReferenceID=1885858 (accessed 2023-07-14).
- (29) Luongo, A.; Brunetti, B.; Vecchio Ciprioti, S.; Ciccioli, A.; Latini, A. Thermodynamic and Kinetic Aspects of Formamidinium Lead Iodide Thermal Decomposition. *J. Phys. Chem. C* **2021**, *125*, 21851.
- (30) Caine, B. A.; Dardonville, C.; Popelier, P. L. A. Prediction of Aqueous p K a Values for Guanidine-Containing Compounds Using Ab Initio Gas-Phase Equilibrium Bond Lengths. ACS Omega 2018, 3, 3835
- (31) Cohen, T. A.; Huang, Y.; Bricker, N. A.; Juhl, C. S.; Milstein, T. J.; MacKenzie, J. D.; Luscombe, C. K.; Gamelin, D. R. Modular Zwitterion-Functionalized Poly(Isopropyl Methacrylate) Polymers for Hosting Luminescent Lead Halide Perovskite Nanocrystals. *Chem. Mater.* **2021**, 33, 3779.
- (32) Huang, Y.; Cohen, T. A.; Sperry, B. M.; Larson, H.; Nguyen, H. A.; Homer, M. K.; Dou, F. Y.; Jacoby, L. M.; Cossairt, B. M.; Gamelin, D. R.; Luscombe, C. K. Organic Building Blocks at Inorganic Nanomaterial Interfaces. *Mater. Horiz.* **2022**, *9*, 61.
- (33) Lu, C. H.; Biesold-Mcgee, G. v.; Liu, Y.; Kang, Z.; Lin, Z. Doping and Ion Substitution in Colloidal Metal Halide Perovskite Nanocrystals. *Chem. Soc. Rev.* **2020**, *49*, 4953.
- (34) Xia, R.; Xu, Y.; Chen, B.; Kanda, H.; Franckevičius, M.; Gegevičius, R.; Wang, S.; Chen, Y.; Chen, D.; Ding, J.; Yuan, N.; Zhao, Y.; Roldán-Carmona, C.; Zhang, X.; Dyson, P. J.; Nazeeruddin, M. K. Interfacial Passivation of Wide-Bandgap Perovskite Solar Cells and Tandem Solar Cells. *J. Mater. Chem. A* **2021**, *9*, 21939.
- (35) Xu, J.; Boyd, C. C.; Yu, Z. J.; Palmstrom, A. F.; Witter, D. J.; Larson, B. W.; France, R. M.; Werner, J.; Harvey, S. P.; Wolf, E. J.; Weigand, W.; Manzoor, S.; van Hest, M. F. A. M.; Berry, J. J.; Luther, J. M.; Holman, Z. C.; McGehee, M. D. Triple-Halide Wide-Band Gap Perovskites with Suppressed Phase Segregation for Efficient Tandems. *Science* 2020, 367, 1097.
- (36) Hou, Y.; Aydin, E.; de Bastiani, M.; Xiao, C.; Isikgor, F. H.; Xue, D. J.; Chen, B.; Chen, H.; Bahrami, B.; Chowdhury, A. H.; Johnston, A.; Baek, S. W.; Huang, Z.; Wei, M.; Dong, Y.; Troughton, J.; Jalmood, R.; Mirabelli, A. J.; Allen, T. G.; van Kerschaver, E.; Saidaminov, M. I.; Baran, D.; Qiao, Q.; Zhu, K.; de Wolf, S.; Sargent, E. H. Efficient Tandem Solar Cells with Solution-Processed Perovskite on Textured Crystalline Silicon. *Science* 2020, 367, 1135.

- (37) Tan, S.; Huang, T.; Yavuz, I.; Wang, R.; Yoon, T. W.; Xu, M.; Xing, Q.; Park, K.; Lee, D.-K.; Chen, C.-H.; Zheng, R.; Yoon, T.; Zhao, Y.; Wang, H.-C.; Meng, D.; Xue, J.; Song, Y. J.; Pan, X.; Park, N.-G.; Lee, J.-W.; Yang, Y. Stability-Limiting Heterointerfaces of Perovskite Photovoltaics. *Nature* **2022**, *605*, 268.
- (38) Kim, H.; Lee, S.-U.; Lee, Y.; Paik, M. J.; Na, H.; Lee, J.; Seok, S. Optimal Interfacial Engineering with Different Length of Alkylammonium Halide for Efficient and Stable Perovskite Solar Cells. *Adv. Energy Mater.* **2019**, *9*, 1902740.
- (39) Shi, Y.; Rojas-Gatjens, E.; Wang, J.; Pothoof, J.; Giridharagopal, R.; Ho, K.; Jiang, F.; Taddei, M.; Yang, Z.; Sanehira, E. M.; Irwin, M. D.; Silva-Acuña, C.; Ginger, D. S. (3-Aminopropyl)Trimethoxysilane Surface Passivation Improves Perovskite Solar Cell Performance by Reducing Surface Recombination Velocity. ACS Energy Lett. 2022, 7, 4081.
- (40) Pratheek, M.; Abhinav, T.; Bhattacharya, S.; Chandra, G. K.; Predeep, P. Recent Progress on Defect Passivation in Perovskites for Solar Cell Application. *Mater. Sci. Energy Technol.* **2021**, *4*, 282.
- (41) Mohd Yusoff, A. R.; Vasilopoulou, M.; Georgiadou, D. G.; Palilis, L. C.; Abate, A.; Nazeeruddin, M. K. Passivation and Process Engineering Approaches of Halide Perovskite Films for High Efficiency and Stability Perovskite Solar Cells. *Energy Environ. Sci.* **2021**, *14*, 2906.
- (42) Wu, G.; Liang, R.; Ge, M.; Sun, G.; Zhang, Y.; Xing, G.; Wu, G.; Liang, R.; Ge, M.; Sun, G.; Xing, G.; Zhang, Y. Surface Passivation Using 2D Perovskites toward Efficient and Stable Perovskite Solar Cells. *Adv. Mater.* **2022**, *34*, 2105635.
- (43) Wu, G.; Liang, R.; Ge, M.; Sun, G.; Zhang, Y.; Xing, G. Surface Passivation Using 2D Perovskites toward Efficient and Stable Perovskite Solar Cells. *Adv. Mater.* **2022**, *34*, 2105635.
- (44) Gong, J.; Hao, M.; Zhang, Y.; Liu, M.; Zhou, Y. Layered 2D Halide Perovskites beyond the Ruddlesden-Popper Phase: Tailored Interlayer Chemistries for High-Performance Solar Cells. *Angew. Chem.* **2022**, *134*, No. e202112022.
- (45) Wang, Q.; Zheng, X.; Deng, Y.; Zhao, J.; Chen, Z.; Huang, J. Stabilizing the A-Phase of CsPbI3 Perovskite by Sulfobetaine Zwitterions in One-Step Spin-Coating Films. *Joule* **2017**, *1*, 371.
- (46) Balakrishnan, S. K.; Kamat, P. V. Au-CsPbBr3 Hybrid Architecture: Anchoring Gold Nanoparticles on Cubic Perovskite Nanocrystals. *ACS Energy Lett.* **2017**, *2*, 88.
- (47) Sension, R. J.; Hudson, B.; Callis, P. R. Resonance Raman Studies of Guanidinium and Substituted Guanidinium Ions. *J. Phys. Chem.* **1990**, *94*, 4015.
- (48) Polavarapu, P. L. Ab Initio Vibrational Raman and Raman Optical Activity Spectra. J. Phys. Chem. 1990, 94, 8106.
- (49) Nelson, C. A.; Zhu, X. Y. Reversible Surface Electronic Traps in PbS Quantum Dot Solids Induced by an Order-Disorder Phase Transition in Capping Molecules. *J. Am. Chem. Soc.* **2012**, *134*, 7592.